Bulk-Heterojunction Electrocatalysts in Confined Geometry Boosting Stable, Acid/Alkaline-Universal Water Electrolysis

Gyu Yong Jang, Sungsoon Kim, Jinu Choi, Jeonghwan Park, SiEon An, Jihyun Baek, Yuzhe Li, Tae-Kyung Liu, Eugene Kim, Jung Hwan Lee, Haotian Wang, MinJoong Kim, Hyun-Seok Cho, Xiaolin Zheng, Jong Suk Yoo,* Kwanyong Seo,* and Jong Hyeok Park*

Alkaline water splitting electrocatalysts have been studied for decades; however, many difficulties remain for commercialization, such as sluggish hydrogen evolution reaction (HER) kinetics and poor catalytic stability. Herein, by mimicking the bulk-heterojunction morphology of conventional organic solar cells, a uniform 10 nm scale nanocube is reported that consists of subnanometer-scale heterointerfaces between transition metal phosphides and oxides, which serves as an alkaline water splitting electrocatalyst; showing great performance and stability toward HER and oxygen evolution reaction (OER). Interestingly, the nanocube electrocatalyst reveals acid/alkaline independency from the synergistic effect of electrochemical HER (cobalt phosphide) and thermochemical water dissociation (cobalt oxide). From the spray coating process, nanocube electrocatalyst spreads uniformly on large scale ($\approx 6.6 \times 5.6$ cm^2) and is applied to alkaline water electrolyzers, stably delivering 600 mA cm^{-2} current for >100 h. The photovoltaic-electrochemical (PV-EC) system, including silicon PV cells, achieves 11.5% solar-to-hydrogen (STH) efficiency stably for >100 h.

1. Introduction

Hydrogen production from electrochemical water splitting is an ecofriendly energy conversion process, which has drawn attention for a few decades.[1–6] Typically, water electrolysis is divided into polymer electrolyte membrane (PEM) electrolysis and anion-exchange membrane (AEM) electrolysis, where acidic and alkaline electrolytes are used, respectively. For PEM water electrolysis, the hydrogen evolution reaction (HER) under acidic conditions is more kinetically favorable than that under alkaline conditions due to the high concentration of protons (H$^+$); but acidic water splitting reveals a critical drawback regarding its poor oxygen evolution reaction (OER) efficiency and the use of rare and valuable noble metal catalysts.[7,8] Since the redox reactions exchange an equal number of electrons at the electrode/electrolyte interfaces, it is important to develop the performance and stability levels of both the anode and cathode to achieve highly efficient H$_2$ production.[9] For this reason, AEM water electrolysis under alkaline conditions has large advantages due to the high efficiency of the full cell because of the low overpotential for the oxygen evolving anode and the accessibility of using transition metal-based materials

G. Y. Jang, S. Kim, T.-K. Liu, E. Kim, J. H. Lee, J. H. Park
Department of Chemical and Biomolecular Engineering
Yonsei University
50 Yonsei-ro, Seodaemun-gu, Seoul 03722, Republic of Korea
E-mail: lutts@yonsei.ac.kr

G. Y. Jang, H. Wang
Department of Chemical and Biomolecular Engineering
Rice University
Houston, TX 77005, USA

S. Kim, J. Baek, Y. Li, X. Zheng
Department of Mechanical Engineering
Stanford University
Stanford, CA 94305, USA

J. Choi, J. S. Yoo
Department of Chemical Engineering
University of Seoul
163 Seoulsiripdae-ro, Seoul 02504, Republic of Korea
E-mail: jsyoo84@uos.ac.kr

The ORCID identification number(s) for the author(s) of this article can be found under https://doi.org/10.1002/aenm.202303924

DOI: 10.1002/aenm.202303924

J. Park, K. Seo
School of Energy and Chemical Engineering
Ulsan National Institute of Science and Technology (UNIST)
50 UNIST-gil, Ulsan 44919, Republic of Korea
E-mail: kseo@unist.ac.kr

S. An, M. Kim, H.-S. Cho
Hydrogen Research Department
Korea Institute of Energy Research
152 Gajung-ro, Daejeon 34129, Republic of Korea

S. An
School of Mechanical Engineering
Yonsei University
50 Yonsei-ro, Seodaemun-gu, Seoul 03722, South Korea

H. Wang
Department of Materials Science and NanoEngineering
Rice University
Houston, TX 77005, USA

H. Wang
Department of Chemistry
Rice University
Houston, TX 77005, USA

**ADVANCED
SCIENCE NEWS**

www.advancedsciencenews.com

**ADVANCED
ENERGY
MATERIALS**

www.advenergymat.de

for each anode and cathode.[8,10] However, the alkaline HER is 2–3 orders of magnitude slower than the acidic HER due to the lack of protons near the surface.[11] Thus, it is necessary to find highly efficient and stable alkaline HER electrocatalysts for the future commercialization of AEM electrolyzers. In addition, recent studies on the development of alkaline water splitting electrocatalysts have explored versatility in various operating environments to reduce the complexity of materials; scholars have investigated pH independency and bifunctionality for HER and OER, respectively.[12–14] Thus, the development of versatile alkaline water splitting electrocatalysts is expected to reduce either the cost or complexity of water electrolyzers.[3,4]

Among the various kinds of transition metal compounds, transition metal phosphide (TMP) is known as a highly active water splitting electrocatalyst material.[15–17] The superior hydrogen evolution activity of TMP is well known, and it originates from various factors: high electronegativities of phosphorous atoms, modification of d-band center and Fermi-level by phosphorous, the Sabatier principle, and so on.[18,19] Moreover, the metal-like conductivity of TMP accelerates charge flow through the electrocatalyst. Since the HER activity of Ni_2P was experimentally confirmed by Schaak et al. in 2013, many TMP-based electrocatalysts have been recently reported, such as Ni_2P, CoP, FeP, MoP, and Cu_3P.[20–24] However, most of the early studies with TMP-based electrocatalysts have involved investigations into the acidic HER due to the sluggish kinetics of the alkaline HER. Moreover, most TMP materials have poor stabilities under alkaline conditions because hydroxide ions attack phosphorous on TMP crystal surfaces, resulting in many difficulties in using this material for alkaline water electrolysis.[25]

To upgrade TMP-based electrocatalysts, some strategies have been suggested, such as providing interfacial effects from heterostructures, doping various elements, and forming multimetallic phases.[26–30] Among these strategies, the interfacial effects from heterostructures have better potential to reach high efficiencies than other strategies because each heterophase material can provide preexisting properties; the synergetic effect emerges at the heterojunction interface.[31–34] For instance, heterojunctions of catalyst materials can modify the electronic structures or surface properties near the interface, remarkably enhancing catalytic properties. Zhou et al. reported interfacial electron transfer between Ni_2P-NiP_2 polymorphs, improving HER performance. Density functional theory (DFT) calculations have proved the electron transfer from metallic Ni_2P to metalloid NiP_2, decreasing proton adsorption energy and increasing conductivity at the interface.[35] However, Fu et al. reported nanometric Ni_5P_4 clusters that are nested on $NiCo_2O_4$ to achieve highly efficient hydrogen production in alkaline media.[36] Researchers have found that $NiCo_2O_4$ promotes the water dissociation Volmer step and provides protons into HER-active Ni_5P_4, resulting in remarkable HER performance under alkaline conditions. However, heterointerface-coupled TMP-based electrocatalysts thus far have shown unsatisfactory efficiencies and stabilities, and their availabilities for various purposes remain unknown.[29]

Herein, we have developed single nanocubes (≈10 nm) that comprise many heterojunction interfaces between the cobalt phosphide and cobalt oxide phases. Our phosphidated cobalt oxide with a nanoscale heterointerface (hereafter PCO-nHI) shows outstanding electrocatalytic hydrogen evolution performance un-

der alkaline conditions, originating from the convergence of highly active electrochemical HER of cobalt phosphide and thermochemical water dissociation of cobalt oxide. Experimental investigations have revealed that the excellent water splitting activity of PCO-nHI requires overpotentials of 162 and 171 mV to reach 100 mA cm^{-2} for acidic and alkaline HER, respectively, implying the capability of acid/alkaline-universal HER. Furthermore, DFT calculations indicate that the simultaneous presence of both CoO and CoP surfaces is crucial, as CoO promotes water dissociation while CoP exhibits high activity in OH* removal. Additionally, CoO remains stable in the presence of CoP, preventing its reduction to pure cobalt. Therefore, the alkaline HER activity of PCO-nHI shows excellent stability over 100 h under various working conditions, which is superior to that of the single cobalt phosphide phase. In addition, because of our spray-coating method, the scalability and applicability of the electrocatalyst is demonstrated, where a 36.96 cm^{-2} catalyst foam is uniformly fabricated; additionally, a high solar-to-hydrogen (STH) efficiency of 11.5% over 100 h is achieved through the help of Si solar cells.

2. Results and Discussion

2.1. Confined Formation of Subnanometer Oxide–Phosphide Heterointerface

The fabrication of the PCO-nHI electrode is illustrated in Figure S1 (Supporting Information). Cobalt oxide (CO) nanocubes were synthesized by a sol-gel reaction with a hot injection method. During the reaction, oleylamine acted as a surfactant and shape-controlling species, producing uniform cobalt nanocubes (≈10 nm) in size, as confirmed by transmission electron microscopy (TEM) measurements (Figure S2, Supporting Information). After the reaction, oleylamine-capped CO nanocubes were precipitated with acetone and centrifuged. The residual pellet was redispersed in toluene, where the oleylamine capping around the CO allowed good dispersion in a nonpolar solvent (Figure S1b, Supporting Information). Due to its good dispersion property, spray coating of the CO solution enabled uniform and conformal coating onto the nickel foam substrate. Large-area (5.6 × 6.6 cm^2) electrodes were easily fabricated (Figure S1c, Supporting Information). The phosphidation process of CO-coated nickel foam was conducted in a tube furnace where NaH_2PO_2 was used as a P source and Ar gas continuously flowed during the reaction. To compare and identify the properties of phosphide materials, we synthesized cobalt phosphide with a general approach; the approach began from cobalt hydroxide materials, and the as-synthesized cobalt phosphide was denoted as CoP.

The crystallography of CO, CoP and PCO-nHI was discovered by high-resolution transmission electron microscopy (HR–TEM). As shown in the inset of **Figure 1a**, a 10 nm CO nanocube was assembled with each particle, and a clear fringe pattern was observed over all the particles. In addition, an inverse fast Fourier transform (IFFT) was used to confirm the phase uniformity along the particle (Figure 1b). The IFFT result of CO implied a clear single phase of CO along the particle. For CoP (Figure 1c), small nanoparticles of approximately 10–20 nm were observed, coagulating to form hexagonal nanodisks (Figure S3g, Supporting
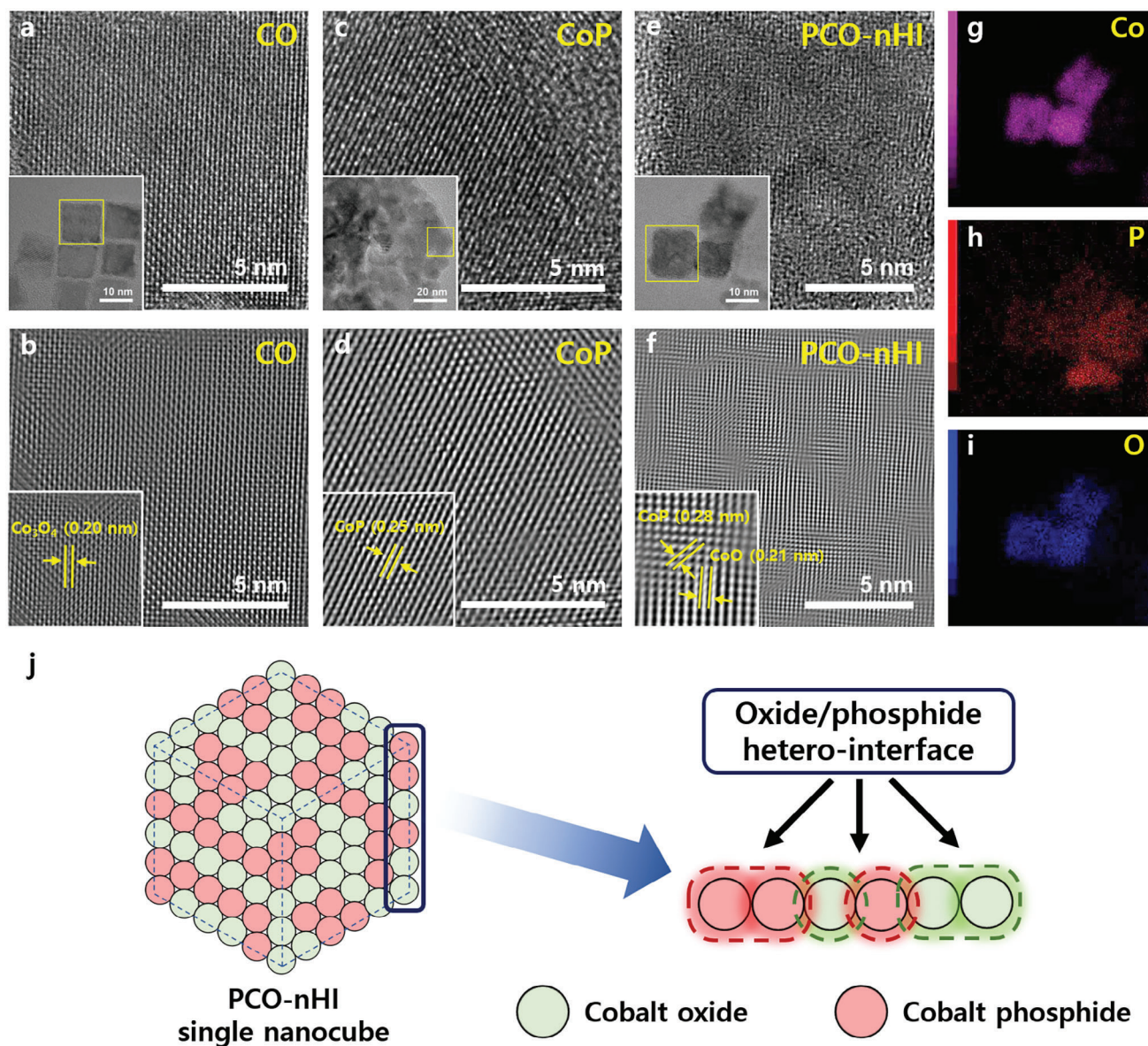
**ADVANCED
SCIENCE NEWS**

www.advancedsciencenews.com

**ADVANCED
ENERGY
MATERIALS**

www.advenergymat.de

Figure 1. Atmoic structure and composition analysis of PCO-nHI single nanocubes. Magnified HR-TEM images of a) CO (yellow box) and b) corresponding IFFT images (inset: a) down-scale HR-TEM image and b) magnified lattice fringe of CO). HR–TEM images of c) CoP and d) corresponding IFFT images. HR-TEM images of e) PCO-nHI and f) corresponding IFFT images. g–i) Corresponding EDS elemental mapping images of PCO-nHI. j) Schematic illustration of the confined oxide/phosphide heterojunction in a single PCO-nHI nanocube.

Information). The IFFT result (Figure 1d) of the nanoparticle revealed a uniform phase of CoP across the particle, ensuring the complete phase transition of the cobalt precursors. Interestingly, we found that PCO-nHI retained its cubic structure in most cases; however, its edges and surfaces were truncated (Figure 1e). The changes in edge and surface were caused by phosphidation, which converted the crystal phase from oxide to phosphide. The crystal phase transition occurred in either the unit cell structure or the bonding length between the atoms, which changed the morphology and surface. Accordingly, CO phosphidation converted the crystal phase along the particles; therefore, the fringe pattern of PCO-nHI was not as clear as that of CO (Figure 1f).

Interestingly, a mixed phase along the PCO-nHI particle by the IFFT process was observed, making it reasonable to assume the co-existence of both cobalt oxide and cobalt phosphide species and the formation of abundant subnanometer heterointerfaces through the randomly mixed crystal phases within the single nanocube (Figure 1f). The heterointerface between oxide and phosphide presumably generated P-O bonding, which was in accordance with the existence of the phosphate peak in the P 2p X-ray photoelectron spectrometry (XPS) spectra discussed later.[37] The elemental distribution of the oxide-phosphide hybrid structure was further confirmed by energy dispersive X-ray spectrometry (EDS, Figure 1g–i). EDS mapping results showed that the
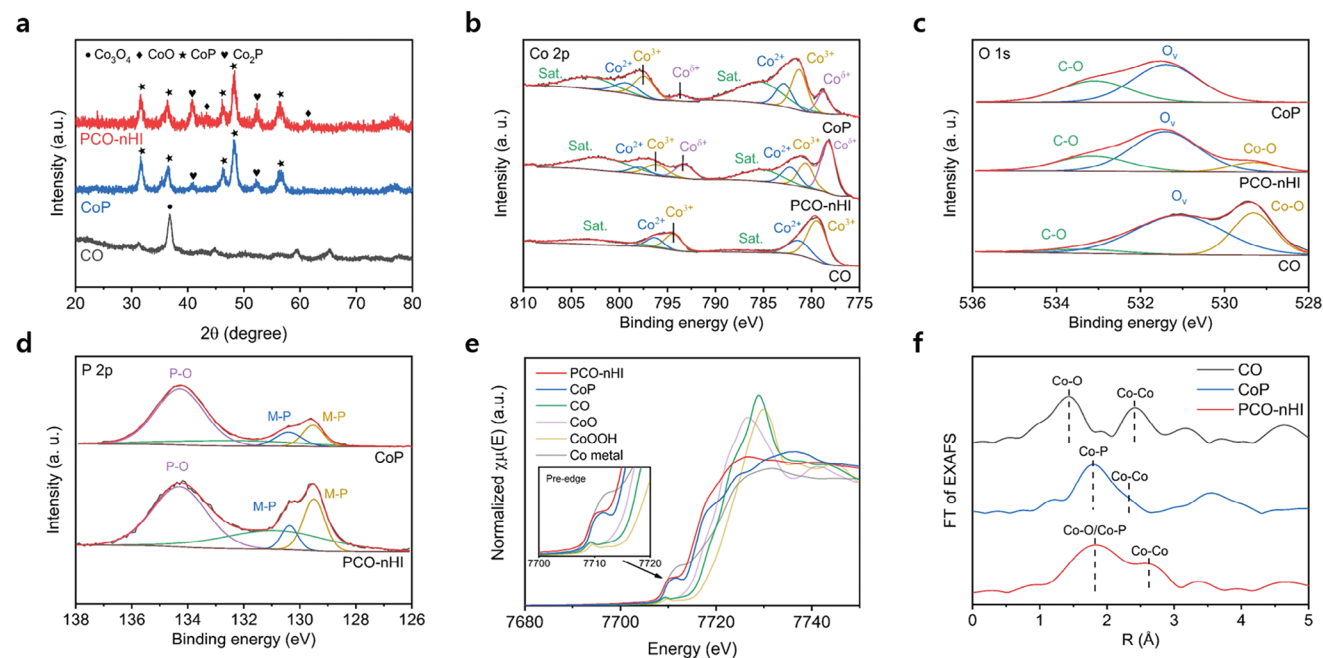
**ADVANCED
SCIENCE NEWS**

www.advancedsciencenews.com

**ADVANCED
ENERGY
MATERIALS**

www.advenergymat.de

Figure 2. Coexistence of oxide and phosphide phases in PCO-nHI nanocubes. a) XRD pattern of CO, CoP, and PCO-nHI. XPS spectra of b) Co 2p, c) O 1s and d) P 2p for three different samples: CO, CoP, PCO-nHI. e) Co K edge XANES spectra of Co metal, CoO, Co_3O_4, CoOOH, CoP and PCO-nHI. (inset: magnified pre-edge of the XANES spectra). f) FT-EXAFS spectra of CO, CoP and PCO.

phosphorous and oxygen elements were in the same position as the cobalt element, implying the evolution of subnanometer interfaces between cobalt oxide and phosphide within the single nanocube. Through the spray-coating method, CO nanocubes were uniformly decorated onto the nickel foam surface, and the following phosphidation process did not change the morphology of the electrode (Figure S3a–f, Supporting Information).

2.2. Identification of Mixed Oxide-Phosphide Phases in PCO-nHI Nanocubes

To understand the crystalline structure of the as-prepared materials, X-ray diffraction (XRD) patterns were measured. XRD pattern of CO showed a remarkable peak at 36.6°, indicating the (311) space direction of the spinel cobalt(II,III) oxide unit cell (**Figure 2a**). However, CoP showed characteristic diffraction peaks at approximately 36.4°, 46.2°, 48.3°, and 56.4°, which corresponded to the (111), (112), (211) and (301) facets of cobalt phosphide. Some minor peaks were at 40.9° and 52.3°, which could be assigned to the (201) and (002) directions of dicobalt phosphide materials generated during phosphidation. It should be noted that the conventional phosphidation process using reactive phosphine gas could lead to various covalency values of phosphide materials in time.[38] For PCO-nHI, the above mentioned cobalt phosphide and dicobalt phosphide peaks were observed, and unindicated peaks were found at 42.5° and 61.6°, which were the (111) and (220) space directions of the periclase cobalt(II) oxide crystal. The conversion of the oxide crystal phase could be caused by a reductive atmosphere during phosphidation. Such mixed oxide and phosphide XRD patterns in PCO-nHI implied that the phosphidation process using the CO nanocubes did not

convert all oxides into phosphide, while it favored the retention of both species together.

XPS was used to further confirm the co-existence of oxide and phosphide materials with respect to the chemical structure. Deconvoluted Co 2p XPS spectra of CO showed Co^{2+} and Co^{3+} mixed states at 781.3 and 779.4 eV, respectively, while that of CoP showed similar Co^{2+} and Co^{3+} mixed states at 782.9 eV and 781.3 eV as well as a characteristic peak at 778.8 eV, implying the existence of cobalt phosphide (Figure 2b).[39] Note that replacement of oxygen atoms in CO to phosphorous to form CoP can result in the positive shifts of Co^{2+} and Co^{3+} states.[40] In the meantime, PCO-nHI showed remarkable phosphide, Co^{2+}, and Co^{3+} peaks at 778.3, 782.2, and 780.61 eV, respectively. Surprisingly, positions of the deconvoluted Co^{2+} and Co^{3+} peaks of PCO-nHI are located between that of CO and CoP, while the phosphide peak is negatively shifted compared to the CoP. This result implies that PCO-nHI is not fully converted to the phosphide phase but it has mixed oxide and phosphide phases, simultaneously.[37,41] To clarify the mixed oxide and phosphide phases in PCO-nHI, portions of the phases were calculated by the deconvoluted XPS result. Firstly, since the oxide phase in PCO-nHI is reduced during the phosphidation, CO was similarly annealed in the tube furnace without a P source and the XPS was measured. The Co 2p XPS spectra of the reduced CO showed Co^{2+} and Co^{3+} states at 780.8 and 779.7 eV, respectively, while the area of Co^{2+} is dominant compared to that of Co^{3+} (Figure S4, Supporting Information). Then, the area percentages of the Co^{2+} and Co^{3+} deconvoluted peaks in CoP, PCO-nHI, and reduced CO were used as constants for the simultaneous equations (Table S1, Supporting Information). Consequently, the portions of oxide and phosphide phases in PCO-nHI were 12.6% and 87.4%, respectively (Table S2, Supporting Information). The

**ADVANCED
SCIENCE NEWS**

www.advancedsciencenews.com

**ADVANCED
ENERGY
MATERIALS**

www.advenergymat.de

O 1s XPS spectra of PCO-nHI exhibited a decreased lattice oxygen peak at 529.2 eV and an increased surface hydroxyl group at 531.3 eV relative to CO; this phenomenon indicated that lattice oxygen in CO was converted to phosphorous during phosphidation, while the surface of PCO-nHI contained a larger amount of oxygen defects due to the introduction of the phosphide phase and reduction of spinel to periclase (Figure 2c). The increased chemisorbed oxygen peak intensity of PCO-nHI at 533.1 eV could be caused by the increased number of oxygen defects that adsorbed a large amount of oxygen species. The tension of decreased lattice oxygen and increased oxygen defects was even stronger in CoP, where the complete disappearance of lattice oxygen peaks at 529.2 eV indicated the complete conversion of cobalt precursors to phosphides. In accordance with the Co 2p and O 1s XPS spectra, the P 2p XPS spectra of PCO-nHI and CoP exhibited phosphide peaks at 129.6 and 130.5 eV, indicating the evolution of phosphide species in PCO-nHI (Figure 2d). The peak at 134.2 eV indicated the phosphate state, which could exist at the interface between the oxide and phosphide of PCO-nHI or at the surfaces of metal phosphides due to their partial oxidation in air.[26,42]

To better understand the unique phase structure in PCO-nHI, X-ray absorption spectra was carried out. Firstly, X-ray absorption near edge structure (XANES) of Co 2K-edge in each CoP, CO and PCO-nHI was measured (Figure 2e). Since the oxidation state of cobalt atom affects all the edge structure in XANES curve, each CoP, CO, and PCO-nHI showed distinguishable curve shapes during the X-ray absorption. The inset figure of XANES graph presents the enlarged graph of pre-edge. PCO-nHI showed the highest pre-edge peak compared to CoP, CO and other reference cobalt compounds except for Co metal, which indicates the lowest electron filling of cobalt atoms in 3d orbital. The HER activity of cobalt phosphide materials increases as the 3d orbital filling degree decreases, due to the strong coupling between Co 3d-orbital and highest occupied molecular orbital (HOMO) of water and reduced Pauli repulsion between Co center electrons and water HOMO electrons. Thus, PCO-nHI is expectable to have a better HER performance compared to bare CoP.[43,44] Meanwhile, rising edges of the Co compounds were located sequentially by the oxidation states of Co. The rising edge of PCO-nHI is the most negatively located compared to the others, which implies the lowest Co oxidation state. Since the oxidation state of CoO, CO, and CoOOH are expected to 3, 2.5, and 2, respectively, the oxidation states of CoP and PCO-nHI were calculated by using the XANES curve. Through the extrapolation of the CoO, CO, and CoOOH oxidation states, as shown in Figure S5 (Supporting Information), the oxidation states of PCO-nHI and CoP were 1.36 and 1.58, respectively.

In line with the XANES study, extended X-ray absorption fine structure (EXAFS) was carried out to reveal the crystallographic information of PCO-nHI. As shown in Figure 2f, EXAFS curves of CO, and CoP showed intrinsic radial distance between Co-O and Co-P bonding at 1.4 and 1.8 Å. Note that the radial distance measured from the EXAFS and the actual distance between two atoms from the crystal unit cell has a difference of ≈0.5 Å due to the phase shift during the Fourier transform of the EXAFS calculation.[45,46] Since the bonding lengths between Co–O and Co–P from the unit cell are 1.916 and 2.307 Å, the radial distance measured from the EXAFS result is reliable (Figure S6,

Supporting Information). To clearly understand the structural information, EXAFS curves of CO, CoP and PCO-nHI were fitted as shown in Figure S7 (Supporting Information) and the parameters were listed in Table S3 (Supporting Information). As a result, PCO-nHI was fitted well with Co–O, Co–P, Co–Co paths since PCO-nHI is a combination of cobalt oxide and phosphide. Interestingly, coordination numbers of Co–O, Co–P, Co–Co paths in PCO-nHI are remarkably reduced compared to CO and CoP. Presumably, this implies that the heterojunction confined in 10 nm nanocube structure generates significant defects along the oxide and phosphide grains, which is in accordance with O 1s XPS spectra result. The defects of the crystal surface are generally considered as better catalytic active sites compared to perfectly crystalline surface, so the defects in PCO-nHI may improve its local catalytic activity. According to HR-TEM, XRD and XPS analysis, oxide and phosphide phases coexisted in PCO-nHI single nanocubes.

2.3. Electrocatalytic HER Activity of PCO-nHI Nanocubes

To examine the electrocatalytic performance of PCO-nHI, the HER was conducted in both acidic and basic electrolytes. In general, alkaline HER suffered from sluggish kinetics due to the lack of protons in basic electrolytes. Thus, improving water dissociation to produce protons and hydroxide ions was the most effective strategy. However, most single compound materials could not simultaneously solve the problems of poor reaction kinetics and slow water dissociation step. As shown in **Figures 3a–c** and S8 (Supporting Information), linear sweep voltammetry (LSV) curves of CO, CoP and PCO-nHI electrodes under acidic (0.5 M H_2SO_4, pH = 0.25) and basic (1 M KOH, pH = 14) conditions were measured. CO required overpotentials of 233.2 and 276.6 mV to achieve a current density of 100 mA cm^{-2} (denoted η_{100}), whereas CoP required 168.2 and 170.6 mV in acidic and basic media, respectively. For CO, LSV curves under acidic and basic conditions showed significant differences due to poor reaction kinetics and slow water dissociation reactions. CoP showed higher HER performance and a smaller overpotential gap between the acidic and basic conditions than CO. However, the kinetic region of CoP near 0.1 V versus reversible hydrogen electrode (RHE) showed a remarkable difference between acidic and basic conditions, implying that the CoP alone was still dependent on the pH conditions. Interestingly, PCO-nHI showed even better HER performance with lower overpotentials than CO and CoP electrodes, showing η_{100} values as low as 162.2 mV and 159.6 mV in acidic and basic media, respectively (Figure S8, Supporting Information). Different from the CO and CoP electrodes, PCO-nHI showed highly similar HER performance characteristics in either acidic or basic electrolytes. The superior HER performance of the PCO-nHI electrode relative to the CoP electrode was believed to be caused by the generation of heterointerfacial properties between cobalt oxide and phosphide on the surfaces of the PCO-nHI nanocubes. The synergetic effects coming from such a unique subnano-oxide-phosphide heterointerface could enhance the water dissociation reaction, providing acid/alkaline-independency. Figure 3d shows a summary of the HER overpotentials of each electrode required to achieve a current density of
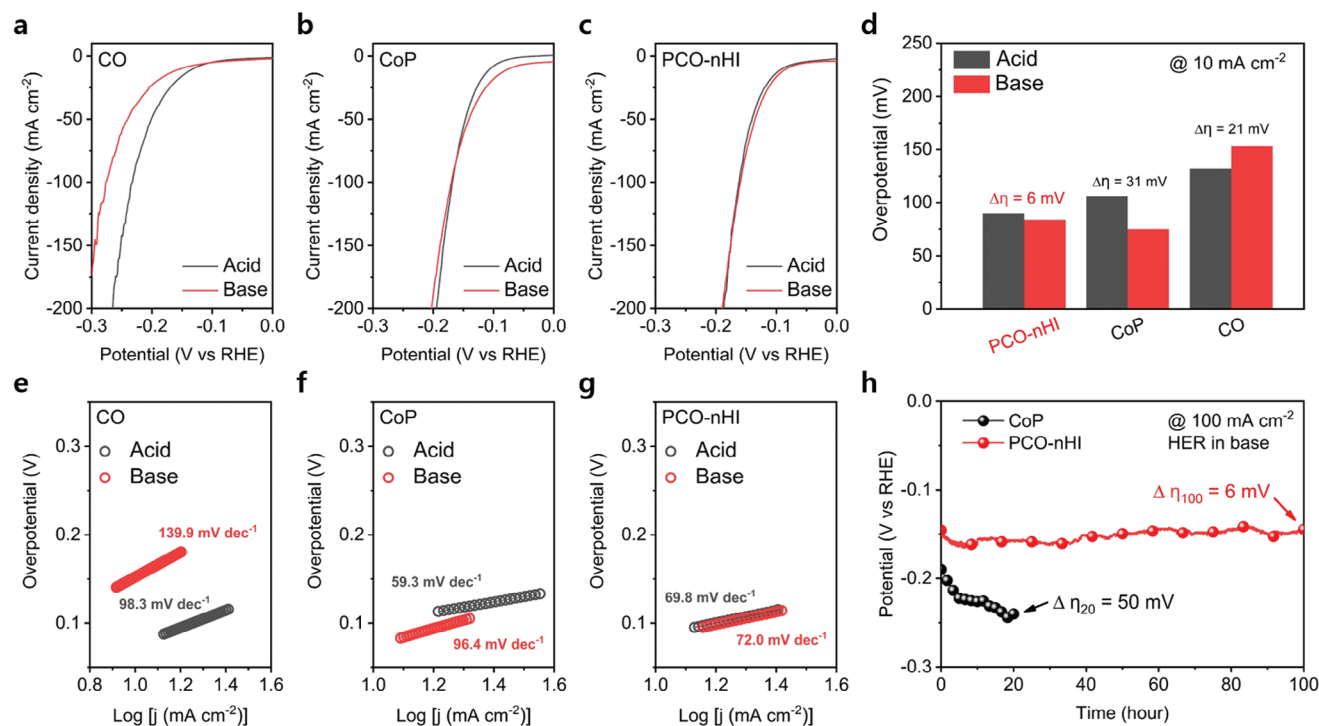
Figure 3. Electrocatalytic HER performance measurements. HER LSV curves of a) CO, b) CoP, and c) PCO-nHI under acidic and basic conditions. d) Overpotential comparison of CO, CoP, and PCO-nHI at a current density of 10 mA cm^{-2}. Tafel slopes corresponding to the LSV curves e) CO, f) CoP, and g) PCO-nHI. h) Long-term time-dependent chronopotentiometric curves of CoP and PCO-nHI at a fixed HER current density of 100 mA cm^{-2} under basic conditions. $\Delta\eta_x$ indicates the overpotential difference of samples after x h of continuous operation.

10 mA cm^{-2}. The graph showed that PCO-nHI had the lowest overpotential difference ($\Delta\eta$) of 6 mV between acidic and basic electrolytes, which definitely outperformed the acid/alkaline-independency of single CO and CoP electrodes; CO and CoP showed $\Delta\eta$ values of 21 and 31 mV, respectively.

To compare the HER activity of electrodes, Tafel slopes under acidic and basic conditions were compared (Figure 3e–g). The slope values of PCO-nHI were lower than that of the CoP and CO electrodes. Interestingly, the Tafel slope of PCO-nHI showed almost identical values under acidic and basic conditions; whereas CoP and CO electrodes showed significant difference. This result implied that the HER performance gap in acid-alkaline was significantly reduced for PCO-nHI, benefitting its universality. To gain further insight into the reaction mechanism of PCO-nHI, electrochemical active surface area (ECSA) estimation and electrochemical impedance spectroscopy (EIS) measurements were conducted (Figure S9, Supporting Information). ECSA measurements showed that PCO-nHI possessed a high ECSA, indicating that it was capable of generating more active sites for the HER. For EIS measurements, PCO-nHI showed the smallest series resistance (R_s) and charge-transfer resistance (R_{ct}) values (2.8 and 20.9 Ω, respectively), each indicating the improved electrochemical conductivity and HER kinetics of PCO-nHI, which was in line with the LSV measurements. The effects of the cobalt and phosphide precursor amounts on the HER performance of PCO-nHI were examined through LSV measurements (Figure S10, Supporting Information). Low Co_3O_4 precursor amount resulted in low coverage of the substrate and over-phosphidation of sam-

ples, whereas the overdeposition of Co_3O_4 precursor leads to incomplete phosphidation and the blocking of active sites for HER, both which lowered the activity. As for phosphide precursor, low amount of phosphide precursor could not generate enough active phosphide species, whereas overphosphidation of Co_3O_4 lead to overdeposition of phosphide species, which blocked the catalytic surfaces and limited the heterointerface effect, resulting in decreased activity. Also, to check the origin of high HER performance of PCO-nHI, we physically mixed the CO and CoP coating solutions and spray-coated them onto nickel foam solutions and measured their alkaline HER activity. As shown in Figure S11 (Supporting Information), the bare co-existence of oxide and phosphide particles was not always beneficial for alkaline HER, which suggested that the controlled formation of hetero-interface structures might be playing a role to enhance HER activity.

The slow water dissociation reaction and poor stability in basic electrolytes was a major issue for cobalt phosphide materials. As shown in Figure 3h, the long-term stability of the CoP electrode was measured at 100 mA cm^{-2} for 20 h. The overpotential of the CoP electrode increased gradually during the operation and reached 231 mV after the test, showing an overpotential increase of 50 mV. Surprisingly, the PCO-nHI electrode showed ultrastable HER operation for 100 h at 100 mA cm^{-2} with a negligible change in overpotential, showing highly improved stability toward HER. LSV measurements of CoP and PCO-nHI before and after stability tests in Figure S12 (Supporting Information) reconfirmed the enhanced stability, where the CoP electrode showed the clear deterioration of performance after

ADVANCED
SCIENCE NEWS

www.advancedsciencenews.com

ADVANCED
ENERGY
MATERIALS

www.advenergymat.de

stability measurements, and the PCO-nHI electrode showed a negligible overpotential difference. Due to the surface reconstruction of metal phosphides under alkaline conditions, XPS analysis of the PCO-nHI electrode after stability measurements indicated certain changes (Figure S13, Supporting Information).[47,48] However, presence of $Co^{\delta+}$ peaks (indicating Co–P bonds), metal-phosphide (M-P) peaks and lattice oxygen peaks ensured that the cobalt oxide-phosphide heterostructure was maintained throughout the reaction process. Moreover, the PCO-nHI electrode showed stable operation for 100 h at 100 mA cm^{-2} under acidic conditions (Figure S14, Supporting Information). However, since cobalt phosphide was a good HER electrocatalyst material under acidic conditions, the CoP electrode showed good stability over 100 h under acidic conditions. Additionally, the acidic/alkaline water splitting performance of the PCO-nHI electrode was superior to most of the reported nickel/cobalt phosphide catalysts to date, while their outstanding acid/alkaline-independency outperformed nearly every catalyst to our knowledge (Tables S4–S6, Supporting Information).

2.4. Theoretical Analysis

Periodic density functional theory (DFT) calculations were utilized to theoretically analyze the heterointerface effect of PCO-nHI on HER. Initially, a Pourbaix diagram was constructed for cobalt in aqueous solution, revealing that across a wide range of pH and under HER conditions ($U < 0$ V$_{RHE}$), cobalt tends to favor the metallic phase, while thermodynamically metal dissolution becomes favorable in the potential range of -0.5–0 V$_{RHE}$ as pH decreases to zero. This indicates that the CO nanocubes, predominantly in the Co_3O_4 phase (Figure 2a), would be reduced to metallic cobalt, primarily on their surface, under HER conditions. However, due to the structural difference between the reduced metallic surface of Co_3O_4 (*Fd-3m*) and pure cobalt metal ($P6_3/mmc$), we chose to analyze the CO nanocubes by considering their reduced surface as Co (110) (*Fd-3m*) rather than Co (0001) ($P6_3/mmc$) in hexagonal close-packed structure. The CoP catalyst was analyzed using slab models for CoP (101) (*Pnma*), which is one of the most stable, highly coordinated, and widely studied facets for both acidic and alkaline HER.[49,50] For the PCO-nHI catalyst, we did not explicitly consider the heterojunction between CoO and CoP (Figure 1), as this would require extremely large unit cells to reasonably minimize the lattice mismatch. Instead, we approximated the reaction energetics at the heterointerface by considering the lower energy values obtained from the comparison of adsorption energies for CoO (110) (*Fm-3m*) and CoP (101) (*Pnma*), under the assumption that adsorbate diffusion is facile across the interface (Figure S15, Supporting Information). Interestingly, thermochemical water dissociation ($H_2O \rightarrow H^* + OH^*$) was found to be highly favorable on the CoO (110) surface until half coverages of H* on the oxygen and OH* on the cobalt sites are reached (Table S7, Supporting Information). Therefore, H* + OH* half-covered surface (Figure S16, Supporting Information) was used to analyze the CoO part of the CoO/CoP heterostructure. Finally, note that, despite CoO being unstable under both acidic and basic HER conditions (Figure S17, Supporting Information) and CoP being unstable mainly under basic HER conditions (Figure 3h), we have assumed that the sub-nanometer-scale CoO/CoP heterostructures remain stable under both acidic and basic conditions due to strong interactions via confinement within nanocubes as confirmed through experiments (Figure 3h).

Figure 4a,b shows the calculated free energy diagrams for HER on Co (110), CoP (101), and CoO (110)/CoP (101) under both acidic (pH = 0) and basic (pH = 14) conditions, respectively. In acidic HER, the Volmer step (H* formation) occurs directly through H+ + e$^-$ → H*, while in basic HER, it can occur both directly ($H_2O + e^- \rightarrow H^* + OH^-$) and indirectly via thermochemical water dissociation ($H_2O \rightarrow H_2O^* \rightarrow H^* + OH^*$) followed by electrochemical OH* desorption (OH* + e$^-$ → OH$^-$). As shown in Figure 4a (acidic HER), the Co (110) surface exhibits an overpotential of 0.17 V, while the CoP (101) and CoO (110)/CoP (101) surfaces, show overpotentials of 0.03 V. This aligns with the experimentally observed overpotential trend of CoP ≲ PCO-nHI < CO (Figure 3d). On the other hand, in Figure 4b (basic HER), it is found that thermochemical water dissociation is difficult on Co (110) and CoP (101), with an activation energy of > 0.5 eV, while it is extremely easy on CoO (110)/CoP (101) with an activation energy of < 0.1 eV, attributed to the highly active CoO phase for water dissociation. Consequently, the direct Volmer route is predicted to be more favorable for Co (110) and CoP (101), while the indirect Volmer route is favored for CoO (110)/CoP (101). As a result, the lowest overpotential of 0.03 V is obtained for CoP (101), while CoO (110)/CoP (101) and Co (110) show overpotentials of 0.06 and 0.17 V, respectively. These findings are consistent with the experimental overpotential trend of CoP < PCO-nHI < CO (Figure 3d).

Thus, the exceptional long-term performance of PCO-nHI in HER under alkaline conditions can be attributed to the synergistic effect of the closely contacted CoP and CoO surfaces. As shown in Figure S15 (Supporting Information), both CoO and CoP surfaces individually face challenges. The CoO surface shows high efficiency in thermochemically dissociating water but lacks the ability to efficiently reduce OH*, potentially leading to OH* poisoning or cobalt hydroxide formation. Conversely, the CoP surface can efficiently reduce OH*, but it faces difficulties in thermochemical water dissociation. Moreover, both CoO and CoP are inherently unstable in alkaline conditions. However, these obstacles are effectively addressed by the sub-nanometer scale interaction between the CoO and CoP phases, achieved through their confinement within nanocubes. Consequently, OH* on the CoO surface can easily migrate to the adjacent CoP surface, ensuring efficient OH* removal and ultimately enhancing the overall performance and stability of the PCO-nHI catalyst.

2.5. Versatility of PCO-nHI Nanocubes

Highly dispersive Co_3O_4 solution enabled exceptionally uniform and scalable spray-coating onto the nickel foam substrate, and the following phosphidation process could enhance the catalytic activity and increase the catalyst adhesion with the substrate. Through the spray coating method, a PCO-nHI electrode was fabricated with a size of 5.6 × 6.6 cm^2; its uniformity was confirmed by dividing the electrode into 15 sections and measuring their respective HER performance. As shown in **Figure 5a,b**, most of the sections showed uniform HER performance with an average

**ADVANCED
SCIENCE NEWS**

www.advancedsciencenews.com

**ADVANCED
ENERGY
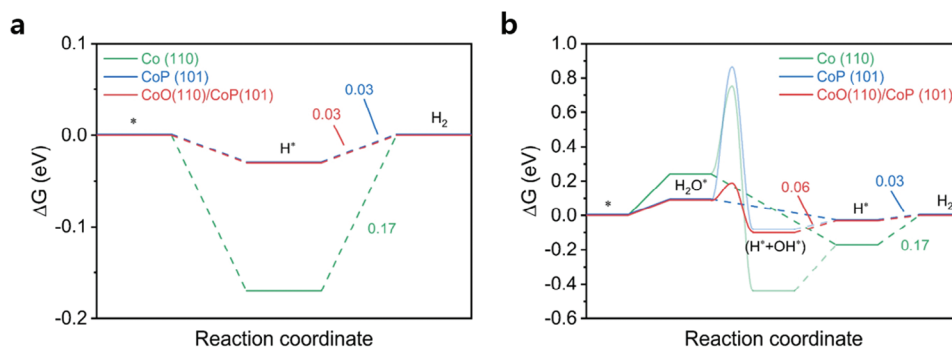MATERIALS**

www.advenergymat.de

Figure 4. DFT calculations. Calculated free energy diagrams for HER under the a) acidic (pH = 0) and b) basic (pH = 14) conditions. Co (110), CoP (101), and CoO (110)/CoP (101) represent the experimentally synthesized CO, CoP, and PCO-nHI catalysts, respectively. Solid and dashed lines indicate thermochemical and electrochemical steps, respectively. Numbers indicate the values of the limiting potentials (reaction energies for the potential determining steps).

overpotential of 168 mV at 100 mA cm^{-2}. As shown in Figure S18 (Supporting Information), a large-scale (36.96 cm^2) PCO-nHI HER electrode with a conventional Ni–Fe LDH OER electrode was applied to a stacked flow cell to supply electrolyte and quickly collect the gas product. As a result, two electrode measurements in a single electrolyzer showed a greatly reduced overpotential (219 mV) at 0.6 A cm^{-2} relative to commercial Ni foam as a HER electrode (Figure 5c). Additionally, the IR region of PCO-nHI showed a similar slope to bare Ni foam, which implied the good conductivity of the PCO-nHI electrode after coating. In addition, we prepared a three-cell short stack alkaline water electrolyzer (AWE) to evaluate its long-term stability under industrial conditions (0.6 A cm^{-2}, 25 wt% KOH at 80 °C). Surprisingly, no appreciable increase in the electrolyzer voltage was observed over 100 h of continuous operation, implying the high stability of our PCO-nHI electrode, even under harsh conditions (Figure 5d).

In line with the uniformity and scalability of the electrode fabrication, the versatility of the PCO-nHI electrode was further examined by using the electrode for the OER. In contrast to the HER, the OER underwent a step-by-step four-electron transfer mechanism, resulting in a significant overpotential from OH$^-$ to O$_2$. OER performance levels of electrodes were measured by LSV measurements (Figure S19a, Supporting Information). PCO-nHI showed improved OER performance compared to CO
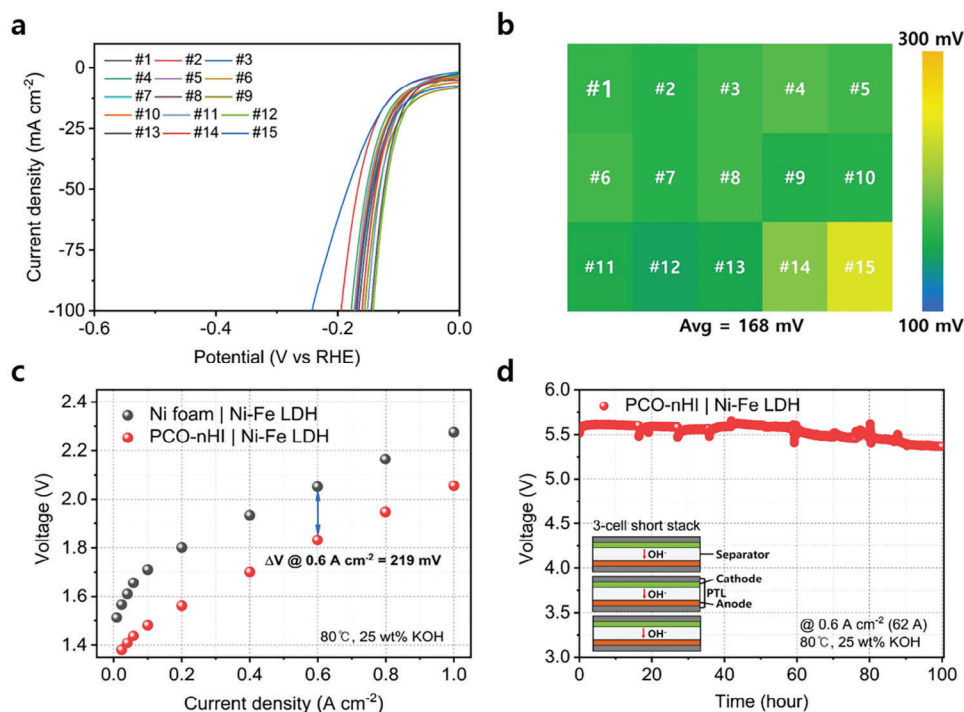

Figure 5. Uniformity and alkaline water electrolysis performance of the large-area (5.6 × 6.6 cm^2) PCO-nHI electrode. a) HER LSV curves measured at 15 different points of the electrode. b) Corresponding color mapping of required overpotentials at a current density of 100 mA cm^{-2}. c) Alkaline water electrolysis performance of PCO-nHI electrodes compared to commercial nickel foam electrodes. d) Continuous long-term alkaline water electrolysis performance of PCO-nHI electrodes at a three-cell short stack electrolyzer configuration.
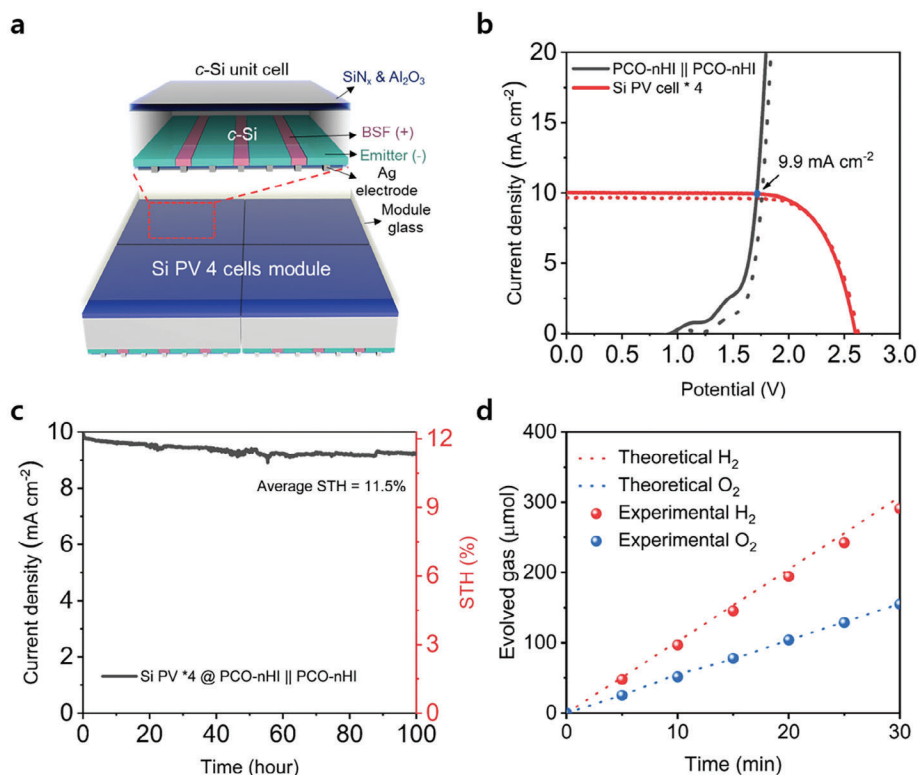
**ADVANCED
SCIENCE NEWS**

www.advancedsciencenews.com

**ADVANCED
ENERGY
MATERIALS**

www.advenergymat.de

Figure 6. Overall water splitting performance of the constructed PV-EC system. a) Schematic illustration of the ABC-structured four-cell Si PV module. b) J–V curves of series-connected Si PV cells and PCO-nHI || PCO-nHI electrodes in a two-electrode setup, under AM 1.5G 100 mW cm^{-2} illumination. Blue dot indicates their intersecting points. Dotted lines represent the J–V curves after stability measurements. c) Long-term unassisted water splitting J–t curves of the PV-EC system under AM 1.5G 100 mW cm^{-2} illumination and their corresponding STH (%) values. d) Faradaic efficiencies of the PV-EC system for the produced gas products.

and CoP, requiring 396.4 mV and 424.4 mV to reach a current density of 100 and 300 mA cm^{-2}. Moreover, fast reaction kinetics of PCO-nHI toward OER were observed by their lowest Tafel slope of 73.9 mV dec^{-1}; they also showed good OER stability at 100 mA cm^{-2} for 100 h (Figure S19b,c, Supporting Information). The overpotential of PCO-nHI was increased by 53 mV after 100 h of operation, which implied great stability against the OER.

As a versatile water splitting electrode, we combined this PCO-nHI electrode for the anode and cathode in a two-electrode configuration and applied it to a Si-based photovoltaic system to realize unbiased, spontaneous PV-EC hydrogen production. To achieve a high STH value in a PV-EC system, the high open-circuit potential (V_{oc}) of solar cells was just as important as the low overpotential of electrocatalysts. In c-Si solar cells, the relatively high V_{oc} was induced by the difference in device architecture. Generally, an all-back-contact (ABC) structure showed a higher V_{oc} than a conventional structure because the ABC structure could mitigate carrier recombination losses by omitting the full-area heavy dopant diffusion at the front surface.[51] Therefore, as shown in **Figure 6**a, an ABC-structured four-cell c-Si PV module was utilized. First, the J–V curves of each PCO-nHI || PCO-nHI and Si PV cell were measured and combined to find the expected operating point. Intersection of the J–V curves of PCO-nHI || PCO-nHI and Si PV cells was at a potential of 1.7 V and a current density of 9.9 mA cm^{-2} (Figure 6b). The connection between PCO-nHI || PCO-nHI and Si PV cells under the

illumination of AM 1.5G 1 SUN simulated light generated spontaneous current flow, which was measured for 100 h of operation. Such PV-EC system showed an average STH efficiency of 11.5% over 100 h, showing ultrastable and efficient operation throughout the measurement (Figure 6c). The observed steady photocurrent was close to the value of the estimated operating point; the J–t curves of the PCO-nHI || PCO-nHI and Si PV cells after 100 h of operation confirmed the stable operation of our PV-EC system. Additionally, the gas evolution from the PV-EC system over 30 min was measured to confirm how well the light-harvested charge carriers participated in the water splitting reaction. Experimentally measured H$_2$ and O$_2$ amounts mostly reached the theoretical amounts by calculation from the amount of charge passed through the cell (Figure 6d,e). This finding implied that the electron successfully participated in the hydrogen and oxygen evolution reaction without being consumed by any other side reactions.

3. Conclusion

In this study, we have successfully developed a highly efficient and versatile water splitting electrode featuring a unique hybrid heterointerface of cobalt oxide and phosphide encapsulated within sub-10 nm nanocubes. The PCO-nHI electrode exhibits exceptional hydrogen evolution reaction (HER) performance, demonstrating acid/alkaline-independency and

**ADVANCED
SCIENCE NEWS**

www.advancedsciencenews.com

**ADVANCED
ENERGY
MATERIALS**

www.advenergymat.de

outstanding stability under both acidic and basic conditions. In contrast, conventional CO and CoP electrodes revealed certain drawbacks, limiting their suitability as feasible HER electrodes. Our density functional theory (DFT) analysis revealed that achieving acid/alkaline-universal HER performance, as seen in PCO-nHI, necessitates the presence of a surface with high water dissociation performance (such as CoO) and high HER activity (such as CoP) within a single catalyst.

Moreover, the coexistence of CoO and CoP in the PCO-nHI catalyst enhances the stability of CoO, preventing its reduction to pure Co metal and enabling it to remain stable during the reaction. Additionally, the PCO-nHI electrode exhibits excellent uniformity due to our spray coating method, enabling large-area fabrication and scale-up measurements. As a result, all 15 points of the as-prepared PCO-nHI electrode demonstrated negligible distribution of overpotentials at 100 mA cm^{-2}, and the large-scale measurement showcased significantly improved HER performance compared to bare Ni foam. Furthermore, our PCO-nHI electrode displayed reasonable oxygen evolution reaction (OER) performance, with an overpotential of 396.4 mV at 100 mA cm^{-2}. Leveraging this performance, two PCO-nHI electrodes were connected to enable overall water splitting, and the setup was integrated with a Si PV cell, forming a spontaneous hydrogen-producing PV-EC system. Remarkably, this PV-EC system achieved a Solar-to-Hydrogen (STH) efficiency of 11.5% over a period of 100 h.

In summary, our PCO-nHI electrode presents a promising solution for efficient and stable water splitting, with its unique heterointerface design offering acid/alkaline-independent performance and potential for scalable applications.

4. Experimental Section

Synthesis of Cobalt Oxide Nanocube Precursor: CO nanocubes were synthesized by using oleylamine as a size and shape controller. In detail, 0.37 g of cobalt(II) nitrate hexahydrate (Sigma Aldrich) was dissolved in 15 mL of 1-hexanol (Sigma Aldrich). Then, 0.27 g of oleylamine (Sigma Aldrich) was added into the solution, and the solution was vigorously stirred for 15 min. The precursor solution was placed in the oil bath, and the temperature was increased to 120 °C. When the temperature of the precursor solution reached 120 °C, 0.7 mL of deionized water was dropped into the solution and stirred for 2 h. After finishing the reaction, the color of the solution changed from green to brown. The CO nanocube solution was cooled by adding acetone, centrifuged at 6000 rpm for 10 min, and redispersed in toluene (Sigma Aldrich) for later use.

Fabrication of CO, CoP, and PCO-nHI Electrocatalysts: Redispersed CO nanocubes were centrifuged at 6000 rpm for 10 min and then dried in an oven at 70 °C for 24 h to obtain CO. PCO-nHI was obtained by phosphorizing CO. Then, 0.5 g of sodium hypophosphite monohydrate (NaH$_2$PO$_2$•H$_2$O, Alfa Aesar) and CO were each placed in an alumina boat upstream and downstream of a quartz tube furnace. Samples were then heated to 300 °C with a heating rate of 5 °C min^{-1} and maintained for 2 h under an Ar atmosphere. Samples were cooled naturally. For comparison, CoP was obtained by a commonly known method.[13,52,53] Briefly, 0.37 g cobalt(II) nitrate hexahydrate (Sigma Aldrich) was dissolved in 15 mL of deionized water. After heating the solution to 45 °C, 16 mL of 0.1 M NaOH solution was added dropwise to obtain cobalt hydroxide products, which were collected by centrifuging at 10 000 rpm for 10 min. After washing with DI water and ethanol repeatedly, they were dried in an oven. Subsequent phosphorization yielded CoP electrocatalysts.

Loading of CO, CoP, and PCO-nHI on Ni Foam: Nickel foam (MTI Korea, 1.6 mm thickness, ≥95% porosity) substrates were cut to 6 × 7 cm^2

and sonicated in 3 M of HCl, deionized water and ethanol for 15 min. In a typical synthesis, the as-synthesized CO and CoP were dispersed in toluene and sonicated for 30 min to form homogenous coating solutions. The concentration of the coating solutions was either used as its original form or diluted to 1/4 of its original concentration. The obtained solutions (12 mL) were then manually airbrushed onto the cleaned nickel foam substrates to form CO and CoP electrodes. The coating areas of the substrates were masked to dimensions of 5.6 × 6.6 cm^2, and the loading amount of electrocatalysts was set to 0.37 ± 0.03 mg cm^{-2}. PCO-nHI electrodes were obtained by phosphorizing the CO electrode.

Structural Characterizations: High-resolution transmission electron microscopy (HR-TEM) images and energy-dispersive spectroscopy (EDS) analyses were acquired with a JEM-F200 field-emission transmission electron microscope with an EDS detector. XRD patterns of the synthesized samples were acquired via an X-ray diffraction analyzer (Ultima IV, Rigaku) with Cu Kα radiation. Morphologies of the samples were studied on a field emission scanning electron microscope (FE-SEM; JEOL-7800F). XPS measurements were performed with a K-alpha instrument from Thermo Scientific Inc. equipped with an aluminum anode (Al Kα = 1486.6 eV) to understand the ionic states of the CO, CoP, and PCO-nHI electrocatalysts. The Co K-edge XAS were performed at the Stanford Synchrotron Radiation Lightsource (SSRL) in SLAC National Accelerator Laboratory. The Co K-edge XAS was measured at beamline 4-1 using a Si(220) monochromator that delivered a 1.5 mm (v) × 3.5 mm (h) X-ray beam at the sample position, and the incident photon energy was calibrated using the transmission-mode XAS spectrum of a Co foil upstream of the incident beam. EXAFS spectra were fitted in a Fourier transform range of 3 - 12 Å^{-1} with a Hanning window between 1- 4 Å^{-1}. During the fitting, the amplitude reduction factor ($S_o{}^2$) was set to 0.85.

Electrochemical Measurements: Electrochemical characterizations and catalytic performance evaluation of all samples were performed using a potentiostat (CH Instruments, CHI 660) with a classic three-electrode setup, utilizing the as-fabricated electrodes as a working electrode, a pt foil as the counter electrode, and a Hg/HgO (in 1.0 M NaOH) or Ag/AgCl (in saturated KCl) as the reference electrode for basic (1.0 M KOH) and acidic (0.5 M H$_2$SO$_4$) electrolytes. Polarization curves were acquired by LSV at a scan rate of 1 mV s^{-1} with iR correction. Chronopotentiometry curves for stability measurements were recorded at a constant current density of 100 mA cm^{-2}. All potentials were normalized with respect to the RHE by using the following Nernst equation: $E_{(RHE)} = E_{(WE)} + E_{(Ref.)} + 0.0591{*}pH$. Electrochemical impedance spectroscopy (EIS) measurements (Gamry Instruments, Reference 600+) were conducted at an overpotential of 100 mV in a frequency range of 100 kH to 1 Hz with an AC amplitude of 5 mV. The electrochemical double-layer capacitance was measured by a CV method. First, potential was applied in the range of 0.0–0.2 V (vs RHE) at different scan rates. After the CVs were measured, half of the current density deviation at 0.1 V (vs RHE) was plotted against the scan rate. The plotted graph was linearly fitted, and its slope was calculated to determine the double-layer capacitance. For overall alkaline water electrolysis, a zero-gap cell was used to evaluate single-cell performance in a 25 wt% KOH at 80 °C. Zirfon (UTP 500, Agfa) was used as the porous separator and Ni foams were used as the porous transport layers for both the anode and cathode. The active area of the electrode was 5.4 cm × 6.4 cm^2.

Si PV Module Fabrication and PV-EC Measurements: Si PV modules were fabricated by arranging and interconnecting as-fabricated all-back-contact (ABC) c-Si unit cells. A transparent ultraviolet (UV)-curable polymer (NOA 63, Norland Products, Inc.) was coated onto the front glass substrate (Asahi glass, AGC Inc.) and arranged ABC c-Si PV cells. Then, the sample was fully cured by UV exposure for 10 min, which formed a transparent handling substrate for the PV module. To interconnect the cells in series, a 500 nm thick Ag interconnection electrode was selectively formed between the unit cells using a shadowing mask through a thermal evaporation process.

Fabricated Si PV modules were electrically connected to the PCO-nHI electrodes with copper wires. Size of each Si solar cell was 0.9 cm^2, yielding a total module area of 3.6 cm^2. Size of PCO-nHI electrodes were 1 cm^2 for both OER and HER. Photocurrent density was calculated based on the

total illuminated area of Si PV modules: 3.6 cm^2. STH efficiency (%) was calculated using the following equation:

$$\eta_{STH}\ (\%) = \left[\frac{(mmol\ H_2\ per\ second) \times \left(237\ 000\ J\ mol^{-1}\right)}{P_{Total}\ \left(mW\ cm^{-2}\right) \times Area\ \left(cm^2\right)}\right]_{AM\ 1.5G}$$

$$= \left[\frac{J_{sc}\ \left(mA\ cm^{-2}\right) \times (1.\ 23\ V) \times \eta_F}{P_{Total}\ \left(mW\ cm^{-2}\right)}\right]_{AM\ 1.5G} \quad (1)$$

Computational Details: Periodic DFT+U (U_{eff} = 3.32 eV for cobalt in cobalt oxides) calculations were performed using PAW pseudopotentials.[54,55] The Vienna Ab-initio Simulation Package (VASP) and RPBE exchange-correlation functional were utilized for all electronic structure and energy calculations with a plane-wave kinetic energy cutoff of 500 eV.[56–59] Convergence was achieved with total energy and force thresholds of less than 10^{-5} eV and 0.02 eV Å^{-1}, respectively. Spin-polarized calculations were performed for Co (*Fd-3m*), CoO (*Fm-3m*), and Co$_3$O$_4$ (*Fd-3m*) but not for CoP (*Pnma*). The spin configurations were set to ferromagnetism for cobalt metal and antiferromagnetism for cobalt oxides.[60–62] A (4 × 4 × 4) Monkhorst-Pack k-point mesh was used for bulk structure calculations of Co, CoO, and Co$_3$O$_4$, whereas a (5 × 3 × 3) mesh was used for CoP.[63] For all surface calculations, (2 × 2 × 4) slab models were employed, with the bottom two layers were fixed and 17 Å of vacuum space along the z-axis, and (4 × 4 × 1) k-point mesh was used. The (110) facet was used for Co, CoO, and Co$_3$O$_4$ surfaces, whereas (101) was employed for CoP, based on previous theoretical studies on the same materials for HER.[49]

Supporting Information

Supporting Information is available from the Wiley Online Library or from the author.

Conflict of Interest

The authors declare no conflict of interest.

Data Availability Statement

The data that support the findings of this study are available from the corresponding author upon reasonable request.

[1] J. A. Turner, *Science* **1999**, *285*, 687.
[2] M. S. Dresselhaus, I. L. Thomas, *Nature* **2001**, *414*, 332.
[3] M. Chatenet, B. G. Pollet, D. R. Dekel, F. Dionigi, J. Deseure, P. Millet, R. D. Braatz, M. Z. Bazant, M. Eikerling, I. Staffell, P. Balcombe, Y. Shao-Horn, H. Schäfer, *Chem. Soc. Rev.* **2022**, *51*, 4583.
[4] T. Zhao, Y. Wang, S. Karuturi, K. Catchpole, Q. Zhang, C. Zhao, *Carbon Energy* **2020**, *2*, 582.
[5] S. Chu, A. Majumdar, *Nature* **2012**, *488*, 294.
[6] G. Glenk, S. Reichelstein, *Nat. Energy* **2019**, *4*, 216.
[7] M. Carmo, D. L. Fritz, J. Mergel, D. Stolten, *Int. J. Hydrogen Energy* **2013**, *38*, 4901.
[8] H. A. Miller, K. Bouzek, J. Hnat, S. Loos, C. I. Bernäcker, T. Weißgärber, L. Röntzsch, J. Meier-Haack, *Sustainable Energy Fuels* **2020**, *4*, 2114.
[9] A. Ray, S. Sultana, L. Paramanika, K. M. Parida, *J. Mater. Chem. A* **2020**, *8*, 19196.
[10] J. Kibsgaard, I. Chorkendorff, *Nat. Energy* **2019**, *4*, 430.
[11] X. Wang, Y. Zheng, W. Sheng, Z. J. Xu, M. Jaroniec, S.-Z. Qiao, *Mater. Today* **2020**, *36*, 125.
[12] R. Boppella, J. Tan, W. Yang, J. Moon, *Adv. Funct. Mater.* **2019**, *29*, 1807976.
[13] Y. Zhao, J. Zhang, Y. Xie, B. Sun, J. Jiang, W.-J. Jiang, S. Xi, H. Y. Yang, K. Yan, S. Wang, X. Guo, P. Li, Z. Han, X. Lu, H. Liu, G. Wang, *Nano Lett.* **2021**, *21*, 823.
[14] J. Mahmood, F. Li, S.-M. Jung, M. S. Okyay, I. Ahmad, S.-J. Kim, N. Park, H. Y. Jeong, J.-B. Baek, *Nat. Nanotechnol.* **2017**, *12*, 441.
[15] A. B. Laursen, K. R. Patraju, M. J. Whitaker, M. Retuerto, T. Sarkar, N. Yao, K. V. Ramanujachary, M. Greenblatt, G. C. Dismukes, *Energy Environ. Sci.* **2015**, *8*, 1027.
[16] J. Tian, Q. Liu, A. M. Asiri, X. Sun, *J. Am. Chem. Soc.* **2014**, *136*, 7587.
[17] F. Yu, H. Zhou, Y. Huang, J. Sun, F. Qin, J. Bao, W. A. Goddard III, S. Chen, Z. Ren, *Nat. Commun.* **2018**, *9*, 2551.
[18] Y. Shi, B. Zhang, *Chem. Soc. Rev.* **2016**, *45*, 1529.
[19] Z. Pu, T. Liu, I. S. Amiinu, R. Cheng, P. Wang, C. Zhang, P. Ji, W. Hu, J. Liu, S. Mu, *Adv. Funct. Mater.* **2020**, *30*, 2004009.
[20] E. J. Popczun, J. R. McKone, C. G. Read, A. J. Biacchi, A. M. Wiltrout, N. S. Lewis, R. E. Schaak, *J. Am. Chem. Soc.* **2013**, *135*, 9267.
[21] B. You, N. Jiang, M. Sheng, M. W. Bhushan, Y. Sun, *ACS Catal.* **2016**, *6*, 714.
[22] P. Xiao, M. A. Sk, L. Thia, X. Ge, R. J. Lim, J.-Y. Wang, K. H. Lim, X. Wang, *Energy Environ. Sci.* **2014**, *7*, 2624.
[23] R. Liu, S. Gu, H. Du, C. M. Li, *J. Mater. Chem. A* **2014**, *2*, 17263.
[24] J. Tian, Q. Liu, N. Cheng, A. M. Asiri, X. Sun, *Angew. Chem., Int. Ed.* **2014**, *53*, 9577.
[25] Y. Zhang, L. Gao, E. J. M. Hensen, J. P. Hofmann, *ACS Energy Lett.* **2018**, *3*, 1360.
[26] T. Kwon, M. Jun, J. Joo, K. Lee, *J. Mater. Chem. A* **2019**, *7*, 5090.
[27] H. Liu, X. Ma, H. Hu, Y. Pan, W. Zhao, J. Liu, X. Zhao, J. Wang, Z. Yang, Q. Zhao, H. Ning, M. Wu, *ACS Appl Mater Interfaces* **2019**, *11*, 15528.
[28] H. Roh, H. Jung, H. Choi, J. W. Han, T. Park, S. Kim, K. Yong, *Appl. Catal., B* **2021**, *297*, 120434.

[29] X. Wang, Y. V. Kolen'ko, X.-Q. Bao, K. Kovnir, L. Liu, *Angew. Chem., Int. Ed.* **2015**, *54*, 8188.

[30] S. M. El-Refaei, P. A. Russo, N. Pinna, *ACS Appl. Mater. Interfaces* **2021**, *13*, 22077.

[31] Y.-Y. Ma, Z.-L. Lang, L.-K. Yan, Y.-H. Wang, H.-Q. Tan, K. Feng, Y.-J. Xia, J. Zhong, Y. Liu, Z.-H. Kang, Y.-G. Li, *Energy Environ. Sci.* **2018**, *11*, 2114.

[32] M. Gong, W. Zhou, M.-C. Tsai, J. Zhou, M. Guan, M.-C. Lin, B. Zhang, Y. Hu, D.-Y. Wang, J. Yang, S. J. Pennycook, B.-J. Hwang, H. Dai, *Nat. Commun.* **2014**, *5*, 4695.

[33] K. Dastafkan, X. Shen, R. K. Hocking, Q. Meyer, C. Zhao, *Nat. Commun.* **2023**, *14*, 547.

[34] H. Liu, R. Xie, Y. Luo, Z. Cui, Q. Yu, Z. Gao, Z. Zhang, F. Yang, X. Kang, S. Ge, S. Li, X. Gao, G. Chai, L. Liu, B. Liu, *Nat. Commun.* **2022**, *13*, 6382.

[35] T. Liu, A. Li, C. Wang, W. Zhou, S. Liu, L. Guo, *Adv. Mater.* **2018**, *30*, 1803590.

[36] T. Zhang, K. Yang, C. Wang, S. Li, Q. Zhang, X. Chang, J. Li, S. Li, S. Jia, J. Wang, L. Fu, *Adv. Energy Mater.* **2018**, *8*, 1801690.

[37] J. Wang, R. Gao, L. Zheng, Z. Chen, Z. Wu, L. Sun, Z. Hu, X. Liu, *ACS Catal.* **2018**, *8*, 8953.

[38] L. Zhang, Y. Chen, G. Liu, Z. Li, S. Liu, S. K. Tiwari, O. Ola, B. Pang, N. Wang, Y. Zhu, *ACS Omega* **2022**, *7*, 12846.

[39] F.-X. Ma, L. Yu, C.-Y. Xu, X. W. Lou, *Energy Environ. Sci.* **2016**, *9*, 862.

[40] G. Tian, X. Liu, S. Song, Q. Zhang, Z. Wang, Y. Liu, Z. Zheng, H. Cheng, Y. Dai, B. Huang, P. Wang, *Chem. - Eur. J.* **2023**, *29*, 202301478.

[41] M. M. Alsabban, M. K. Eswaran, K. Peramaiah, W. Wahyudi, X. Yang, V. Ramalingam, M. N. Hedhili, X. Miao, U. Schwingenschlögl, L.-J. Li, V. Tung, K.-W. Huang, *ACS Nano* **2022**, *16*, 3906.

[42] F.-S. Zhang, J.-W. Wang, J. Luo, R.-R. Liu, Z.-M. Zhang, C.-T. He, T.-B. Lu, *Chem. Sci.* **2018**, *9*, 1375.

[43] H. Yan, C. Tian, L. Wang, A. Wu, M. Meng, L. Zhao, H. Fu, *Angew. Chem., Int. Ed* **2015**, *54*, 6325.

[44] Y. Men, Y. Tan, P. Li, X. Cao, S. Jia, J. Wang, S. Chen, W. Luo, *Appl. Catal., B* **2021**, *284*, 119718.

[45] M. R. Antonio, in *Encyclopedia of Materials Characterization* (Eds: C. R. Brundle, C. A. Evans, J. S. Wilson), Elsevier, Amsterdam, **1992**, pp. 214–226.

[46] T. Guoxin, Z. Yongjun, X. Jingming, Z. Ping, H. Tiandou, X. Yaning, Z. Jing, *Inorg. Chem.* **2003**, *42*, 735.

[47] X. Wei, S. Zhang, X. Lv, S. Dai, H. Wang, M. Huang, *Appl. Catal., B* **2024**, *345*, 123661.

[48] L. Su, X. Cui, T. He, L. Zeng, H. Tian, Y. Song, K. Qia, B. Y. Xia, *Chem. Sci.* **2019**, *10*, 2019.

[49] J. Kibsgaard, C. Tsai, K. Chan, J. D. Benck, J. K. Nørskov, F. Abild-Pedersen, T. F. Jaramillo, *Energy Environ. Sci.* **2015**, *8*, 3022.

[50] Z. Wang, Y.-R. Zheng, J. Montoya, D. Hochfilzer, A. Cao, J. Kibsgaard, I. Chorkendorff, J. K. Nørskov, *ACS Energy Lett.* **2021**, *6*, 2268.

[51] A. Richter, R. Müller, J. Benick, F. Feldmann, B. Steinhauser, C. Reichel, A. Fell, M. Bivour, M. Hermle, S. W. Glunz, *Nat. Energy* **2021**, *6*, 429.

[52] J. Yang, H. Liu, W. N. Martens, R. L. Frost, *J. Phys. Chem. C* **2010**, *114*, 111.

[53] Y. Xiao, X. Chen, T. Li, Y. Mao, C. Liu, Y. Chen, W. Wang, *Int. J. Hydrogen Energy* **2022**, *47*, 9915.

[54] S. L. Dudarev, G. A. Botton, S. Y. Savrasov, C. J. Humphreys, A. P. Sutton, *Phys. Rev. B* **1998**, *57*, 1505.

[55] P. E. Blöchl, *Phys. Rev. B* **1994**, *50*, 17953.

[56] G. Kresse, J. Hafner, *Phys. Rev. B* **1993**, *47*, 558.

[57] G. Kresse, J. Furthmüller, *Comput. Mater. Sci.* **1996**, *6*, 15.

[58] G. Kresse, J. Furthmüller, *Phys. Rev. B* **1996**, *54*, 11169.

[59] B. Hammer, L. B. Hansen, J. K. Nørskov, *Phys. Rev. B* **1999**, *59*, 7413.

[60] R. J. Makkonen, *Suom. Kemistil. A* **1962**, *35*, 230.

[61] K. W. Park, A. M. Kolpak, *J. Catal.* **2018**, *365*, 115.

[62] J. Chen, A. Selloni, *Phys. Rev. B* **2012**, *85*, 085306.

[63] H. J. Monkhorst, J. D. Pack, *Phys. Rev. B* **1976**, *13*, 5188.